Common-mode plasmon sensing scheme as a high-sensitivity compact SPR sensor

Hugo Bruhier, Julie Dutems, Emilie Laffont, Nicolas Crespo-Monteiro, Isabelle Verrier, Olivier Parriaux, Pierre Berini, Yves Jourlin

Optics Letters

Common-mode plasmon sensing scheme as a high-sensitivity compact SPR sensor

Hugo Bruhier,[1] Julie Dutems,[1] Emilie Laffont,[1,2,3,4] Nicolas Crespo-Monteiro,[1] Isabelle Verrier,[1] Olivier Parriaux,[1] Pierre Berini,[2,3,4] and Yves Jourlin[1,*]

[1]Université Jean Monnet Saint-Etienne, CNRS, Institut d'Optique Graduate School, Laboratoire Hubert Curien UMR CNRS 5516, F-42023 Saint-Etienne, France
[2]Department of Physics, University of Ottawa, Ottawa, Canada
[3]Nexus for Quantum Technologies Institute, University of Ottawa, Ottawa, Canada
[4]School of Electrical Engineering and Computer Science, University of Ottawa, Ottawa, Canada
*yves.jourlin@univ-st-etienne.fr

Received 19 December 2022; revised 18 May 2023; accepted 5 June 2023; posted 7 June 2023; published 7 July 2023

A deep metal grating enables quasi-phase-matched simultaneous excitation of two counterpropagating surface plasmon modes by means of its +1st and –2nd diffraction orders. The resulting angular reflection spectra of the scattered –1st and zeroth orders exhibit three interleaved zeros and maxima in a range centered around the Littrow angle. The spectra differ thoroughly from the usual reflection dip resulting from single-order plasmon coupling that produces strong absorption. The zeroth and –1st orders exhibit two crossing angles enabling high-sensitivity common-mode detection schemes designed to reject variations in source power and environmental noise. The proof of concept and experimental assessment of this new surface plasmon resonance (SPR) sensing scheme are demonstrated by monitoring gases in a pressure-controlled chamber. A limit of detection (LOD) of 2×10^{-7} refractive index unit (RIU) was achieved.

https://doi.org/10.1364/OL.483692

Introduction. The present work deals with the detection of a (bio)chemical or physical event by an optical wave propagating along a surface excited by free-space coupling. The surface wave is a surface plasmon polariton at a metal–dielectric interface, as shown in a previous work [1] for the potential measurement in electrolytes, and by Liedberg *et al*. [2] for biosensing. The method of coupling to surface plasmons has mainly been that of the Kretschmann–Raether configuration [3]. An incident wave tunnels through a thin metal film deposited on a high refractive index medium and is coupled to the plasmon that propagates along the interface with the sensing medium. The monolithic grating coupling approach [4] provides far richer functionality, particularly by applying the distinctive effect of resonant reflection [5,6]. On this point, Dostálek *et al*. authored an exhaustive review of grating-coupled plasmon sensors [7] which was completed by another recent review by Cao *et al*. [8]. Even though the surface plasmon resonance (SPR)-based prism interrogation is much more developed commercially, it suffers from the compactness limits of this configuration, whereas the grating-based SPR configuration can be considered as promising for its integration and its large volume fabrication potential. The physical or (bio)chemical measurand is usually monitored by locating the reflection peak (in the case of a dielectric waveguide) or dip (in the case of a plasmon) in the wavelength or in the angular zeroth order Fresnel reflection spectra. Recently, sensitivity as high as 30,000 nm per refractive index unit (RIU) was achieved for biomolecule detection [9], 1500 nm/RIU in aqueous media [10] and 85.65°/RIU for various analyte sensing applications [11]. Whereas the distinctive effect of resonant reflection from a grating-coupled dielectric waveguide mode cannot manifest itself in a plasmon mode because of its large dissipative loss (except in the symmetrical thin metal film system propagating long-range plasmon mode [12]), the plasmon coupling effect proposed here produces quasi-lossless reflection peaks of the zeroth and –1st orders. This effect, termed "Plasmon-triggered switching effect" by the authors, was discovered a few years ago while searching for new anti-counterfeiting metallic features for innovative security solutions using a thin metal grating layer involving plasmon coupling [13]. The effect occurs only in the very particular case of deep metal gratings. Such an effect was recently used to measure the refractive index of aqueous solutions [14]. The aim of the present paper is to highlight the preeminence of the switching effect in a sensor configuration by providing a more detailed description of the principle and of the performances of the sensor when used to measure variations in the refractive index. We demonstrate the ability of the sensor to detect variations in the air refractive index via a pressure change with enhanced accuracy thanks to appropriate digital processing. Our description is completed by a video (see Visualization 1) that illustrates plasmon coupling. The following section presents a simplified electromagnetic phenomenology of the plasmon-mediated interference effect, followed by its experimental demonstration as a refractive index sensor operating with gases to determine the limit of detection (LOD) for refractive index sensing.

Electromagnetic model of zeroth/–1st order plasmon-triggered switch used as an SPR sensor. The new plasmon resonance effect described here occurs on a metal grating

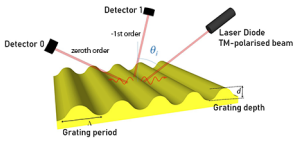

Fig. 1. Common-mode plasmon sensing scheme.

structure of period Λ very similar to the usual diffractive plasmon couplers from monochromatic TM free-space waves under oblique incidence θ_i in a medium of refractive index n. The basic coupling scheme by a diffracted order m is described by Eq. (1) that gives the plasmon propagation constant β as a function of the resonant incidence angle θ_p at wavelength λ:

$$\beta = n\frac{2\pi}{\lambda}\sin\theta_p + m\frac{2\pi}{\Lambda}. \quad \textbf{(1)}$$

However, there are two important novel characteristics that make the approach completely different from the usual SPR coupling at the metal–dielectric interface. The first concerns the opto-geometrical conditions, i.e., the relationship between wavelength λ and the grating period Λ: their ratio is such that the -1^{st} order Littrow angle θ_L given by $\sin(\theta_L) = \lambda/(2n\Lambda)$ corresponding to the incidence angle which is equal to the -1^{st} reflected order angle, is smaller than 30° whatever the value of n, as illustrated in Fig. 1. This is to ensure that the zeroth and –1st reflected diffraction orders only have a propagating character in the incidence medium; the higher +1st and –2nd orders have to be evanescent to prevent the reflected power being shared between more than two orders.

In the above condition, an angular scan of the incident wave exhibits exactly two dips in the reflected angular spectrum due to the forward propagating plasmon excitation by the +1st grating order, and the backward propagating plasmon by the –2nd order.

The second novel characteristic concerns the very nature of the coupling mechanisms involved. The grating depth (d) used in most plasmon applications that exhibit a reflection dip is a few tens of nanometers [15] for operations in the visible or near-infrared (NIR) range. A greater depth generates a fundamentally different reflection spectrum. Numerical results using the Chandezon method [16,17] applied to a sinusoidal grating with a period of 850 nm illuminated by a TM-polarized 850-nm wavelength beam are shown in Figs. 2(a) and 2(b) in the case where the sensing medium is air ($n = 1$). The angular reflection spectra of the zeroth and –1st orders are observed to evolve with the grating depth: the two well-separated standard reflection dips at the synchronous plasmon excitation angle at small grating depth, in the range of 40 nm (i.e., when the phase matching condition between the incident k-vector, the grating K-vector, and the propagation constant of the plasmon is satisfied) transform into broad zeroth order constructive interference maxima at the previous synchronous plasmon excitation angles with cancelation of the –1st order under the Littrow angle [18]. This is an effect of the non-negligible –3rd grating order at large depth that couples the two couterpropagating plasmon modes. The red angular spectra in Fig. 2(c) at the optimal grating depth (around 280 nm) thus exhibit three interleaved zeros and maxima with two crossing points (cross marks), at angles of 13° and 62°, respectively. The video (see Visualization 1) describes the angular spectrum and the E-field amplitude near the grating–air interface.

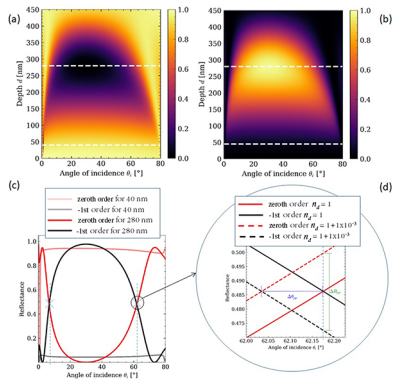

Fig. 2. Efficiency (color bar) versus grating depth and incidence angle for (a) zeroth reflected order, and (b) –1st reflected order for a sinusoidal gold grating ($\varepsilon = -32 + 1.26j$ at wavelength λ=850 nm) of period Λ=850 nm with air cover. (c) Angular spectra of the –1st and zeroth reflected orders for 40 nm and 280 nm grating depths, and (d) zoom on (c) at the crossing point θ_i= 62° with changes in the refractive index cover medium in the range of 10^{-3}.

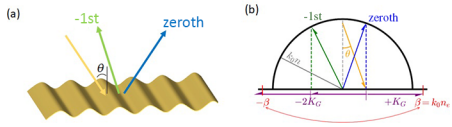

Fig. 3. (a) Incident beam and reflected zeroth and –1st orders in direct space. (b) Diagram of Ewald's reciprocal space; counterpropagating plasmon modes of propagation constant β, K_G: grating constant with $3K_G \gtrsim \beta$.

There is almost no trace of plasmon absorption loss in Fig. 2(c). The two maxima of the zeroth order correspond to plasmon mode excitation where the absorption loss is even smaller than at the maximum corresponding to the –1st order under Littrow incidence. This balanced spectrum pattern with large maxima occurs as long as no higher diffraction orders have a propagating character over the angular range considered. The plasmon mode propagation constant $\beta = n_e k_0$ (n_e is the plasmon effective index) is so close to the wave vector $k_0 = 2\pi/\lambda$ in the incidence medium that the following relationship must hold between the grating K-vector ($K_G = 2\pi/\Lambda$) and the propagation constant β: $3K_G \gtrsim \beta$ over the angular range as sketched in the reciprocal plane in Fig. 3(b).

A coupled-mode phenomenological model was developed [19] to account for this depth-dependent angular spectrum and for the absence of excess loss. The explanation is illustrated in Fig. 3 using the reciprocal space diagram in Fig. 3(b) and the corresponding direct space of the propagating orders in Fig. 3(a).

The reflection spectra result from generalized interference in the zeroth and –1st order directions between coupled and re-radiated plasmon fields with the major contribution of the strong 3rd order intra-plasmonic coupling between counterpropagating plasmon modes due to the large grating depth despite the slight phase mismatch between their propagation constant $\pm\beta$ and the spatial frequency $3K_G$ of the 3rd grating order.

The large grating depth induces a large radiation coefficient that prevents the plasmon modes having a long propagation length before being re-radiated into the incident medium, thus limiting plasmon absorption loss. An increase in the cover

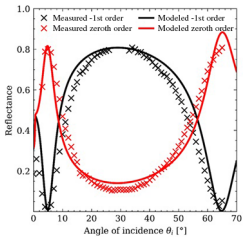

Fig. 4. Reflectance of the zeroth (red) and −1st (black) orders as incidence angle θ_i varies from 0 to 64°.

medium refractive index, or the presence of a nano-(bio or functional) layer at the surface, causes the angular pattern shown in Fig. 2(c) to shrink. However, this pattern exhibits two crossing points between zeroth and −1st order spectra at two incidence angles [Fig. 2(c)] where the two reflected power signals can be measured in two directions simultaneously with a quasi-linear relationship between measurand and detected power. Sensitivity is then proportional to the slopes of the crossing curves. As illustrated in Fig. 2(d), refractive index changes of 10^{-3} in the medium bounding the metal–air interface will lead to a shift of the angular spectra of $\Delta\theta_{pp}$. For a specific crossing point (e.g., the angle on the right-hand side of the Littrow angle, that is θ= 62°), efficiencies of the zeroth and −1st reflected orders will vary linearly in opposite directions, which will correspond to a differential efficiency measurement of ΔR_{pp}. This operating angle represents scanning-less common-mode detection, with rejection of source fluctuations and environmental perturbations. This motivates the use of such phenomena as an optical sensor, comprising at least two fixed detectors and a collimated laser diode (as illustrated in Fig. 1). The experimental assessment of the proposed sensor scheme as a refractometric sensor, measuring variations in the air refractive index in a pressure-controlled chamber, is described in the next section.

Experimental assessment. The sample tested here was a sinusoidal photoresist grating of 850 nm period and 230 nm full depth printed by laser interference lithography and subsequently coated with a gold layer 80 nm thick by thermal evaporation (see Supplement 1, S1: Fabrication process). Modeling confirmed the gold was thick enough to produce the same optical response as that obtained with thicker layers. The design of the grating produces an optimized angular spectrum according to Fig. 2(c) and two crossing points on either side of the Littrow angle. The first experiment consisted of plotting the angular spectrum of the zeroth and −1st reflected orders under ambient conditions, scanning the incidence angle from 0 to 64°. Using a rotation stage and a photodetector, the reflectances of both orders were measured versus the incidence angle of the TM-polarized collimated beam from a 850-nm stabilized semiconductor laser diode. Figure 4 plots measured efficiencies (crosses) and simulated efficiencies (solid lines) using Chandezon's method. Modeling considers the real grating profile obtained by atomic force microscopy (AFM) measurements, in particular the roughness of the gold coating, which was recently demonstrated as a key parameter especially for deep metallic gratings [20]. The roughness shifts and broadens the resonances, thereby shifting the second crossing point to a smaller angle. However, the angular response keeps the same tendency. Figure 4 shows that the measured spectra are very close to the simulated ones, considering the grating roughness measured to an average value of 7 nm.

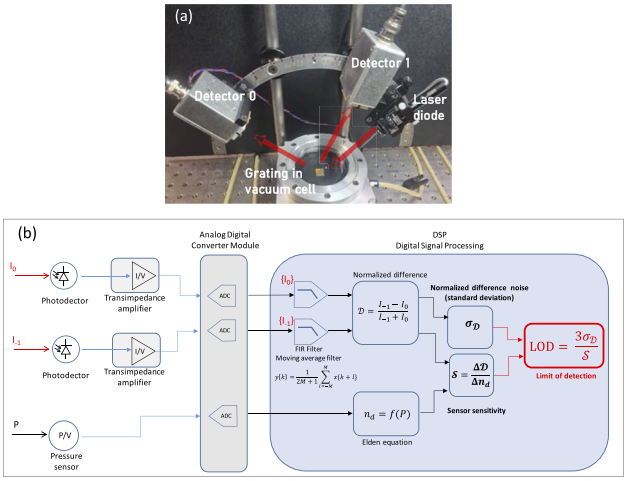

Fig. 5. (a) Photograph of the optical sensing setup. (b) Schematic diagram of signal acquisition and processing to calculate the LOD.

The grating was then inserted into a custom-made vacuum chamber with a window such that the air pressure could be varied, thereby slightly altering the refractive index of the sensing medium. As illustrated in Fig. 5(a), the collimated TM-polarized beam issued from the laser diode, identical to the one previously used to measure the angular spectra in Fig. 4 and located outside the pressure chamber, impinges on the metal grating. The incidence angle corresponds to one of the measured crossing points (~55°). This incidence angle enables both detectors to be positioned on the same side of the incident beam (as illustrated in Fig. 1). The detectors—Si photodiodes integrated with a transimpedance amplifier—convert the output currents (I_0 and I_{-1}) into voltages.

As shown in Fig. 5(b), analog voltages were acquired at a sampling frequency of 2.5 kHz and converted into digital data using an analog-to-digital (ADC) converter then low-pass filtered (sliding average filter) to improve the signal-to-noise ratio. The output signal is the normalized difference of these filtered data, thereby increasing sensor sensitivity compared to the simple difference (see Supplement 1, S2: Signal processing).

In this proof of concept, the variation in the refractive index was achieved by varying the air pressure in the chamber using a vacuum pump at constant temperature following the Edlén equation relating refractive index to pressure (linearly) [21]. There is therefore a direct function between the detected signal and pressure, assuming a linear response of the detectors. Pressure was measured using a piezo-resistive sensor inserted into the vacuum chamber, acquired and converted into digital data using the same ADC module.

The sensitivity ($\mathcal{S}$) of the sensor was calculated using Eq. (2) from the normalized difference ($\mathcal{D}$) between the signals from the two photodetectors that vary in opposition while the refractive index of the air varies. The expected change in the refractive index of the air was computed using the Edlén equation [21] and the measured change in pressure in the chamber. This enabled measurement of the direct and real-time difference in the two signals, canceling common perturbations, assuming identical detectors (see Supplement 1, S3: Metrology):

$$\mathcal{S} = \frac{\Delta\mathcal{D}}{\Delta n_d}. \tag{2}$$

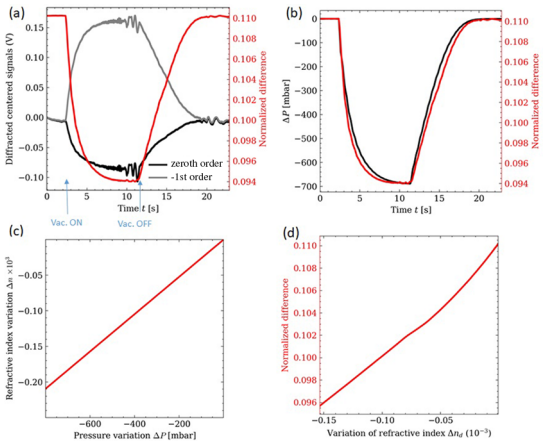

Fig. 6. (a) Signals of the zeroth (black) and –1st (gray) reflected orders and normalized difference (red) versus time. (b) Variation in pressure (black) and normalized difference (red) versus time. Calculated transfer function: (c) refractive index variation versus pressure variation, and (d) normalized difference versus variation in the refractive index.

The LOD was then calculated using Eq. (3) with the sensitivity [Eq. (2)] and the measured noise taken as the standard deviation $\sigma_{\mathcal{D}}$ of the normalized difference ($\mathcal{D}$) over time:

$$\mathrm{LOD} = \frac{3\sigma_{\mathcal{D}}}{\mathcal{S}}. \tag{3}$$

Figure 6(a) plots the photodetector signals and the corresponding normalized difference, while Fig. 6(b) plots the variation in pressure and the normalized difference acquired during the experiment, which consisted of dropping the pressure from 1 atm (1015 mbar) at $t = 3$ s to 300 mbar (up to $t = 12$ s) in the vacuum chamber. The two graphs show that the normalized and measured difference in pressure are very close, despite small delays which are explained by the response time of the degassing and desorption of molecules adsorbed at the surface of the gold grating. Note that the common-mode noise and parasitic perturbations of the two diffracted orders near $t = 10$ s and $t = 20$ s are canceled using the difference [Fig. 6(a)]. Figure 6(c) plots the refractive index versus the pressure variation [at 25°C and 35% relative humidity (HR)] from the Edlén equation and Fig. 6(d) is the normalized difference of the signals versus the change in refractive index, the latter obtained using the measured pressure.

The slope of this curve gives the experimental sensitivity ($\mathcal{S}$) around 96 RIU^{-1} with a correlation coefficient R^2 of 0.992. Finally, the LOD was obtained from the calculated sensitivity and the standard deviation ($\sigma_{\mathcal{D}}$) of the normalized difference signal according to Eq. (2) using the measured standard deviation ($3\sigma_{\mathcal{D}}$) of 5.7×10^{-6}. The experimentally achieved LOD is 2×10^{-7} RIU, which is state of the art for SPR-based sensors, while offering a simplified and compact optical scheme.

Conclusion. Our results demonstrate a new SPR-based approach that allows high resolution, yielding to an LOD in the range of 10^{-7} RIU, and very simple sensor implementation based on the different intensity measurement of diffracted orders. The approach is based on the switch effect exploiting low-loss surface plasmon detection between two propagating reflected orders, which occurs only in the very particular case of deep metal gratings. Further improvements to the sensor can be envisaged, mainly miniaturization and transducer optimization and fabrication, as well as improvements to signal processing to increase the sensitivity and the LOD. This is a promising approach for the production of new cost-effective, high-sensitivity, and compact optical sensors.

Funding. Agence Nationale de la Recherche CAPTAIN Project (ANR-18-CE04-0008), LABEX MANUTECH-SISE (ANR-10-LABX-0075) EUR MANUTECH SLEIGHT (ANR-17- EURE-0026); Centre National de la Recherche Scientifique (CNRS) French RENATECH+ Network on the NanoSaintEtienne Technological Platform.

Acknowledgments. The authors thank UJM engineers Colette Veillas for help with the optical bench, and Frédéric Celle and Frédéric Arnould for providing the electronic and mechanical parts of the sensor, respectively.

Disclosures. The authors declare no conflicts of interest.

Data availability. Data underlying the results presented in this paper are not publicly available at this time but can be obtained from the authors upon reasonable request.

Supplemental document. See Supplement 1 for supporting content.

REFERENCES

1. J.G. Gordon II and S. Ernst, Surf. Sci. **101**, 499 (1980).
2. B. Liedberg, C. Nylander, and I. Lunström, Sens. Actuators **4**, 299 (1983).
3. E. Kretschmann and H. Raether, Zeitschrift für Naturforschung A **23**, 2135 (1968).
4. K. Tiefenthaler and W. Lukosz, Opt. Lett. **9**, 137 (1984).
5. N. M. Lyndin, V. A. Sychugov, A. V. Tishchenko, and B. A. Usievich, "Analytical methods and apparatus employing an optical sensor device with refractive index modulation," U.S. patent 6,218,194B1 (17 April 2001).
6. Y. Fang, A. M. Ferrie, N. H. Fontaine, J. Mauro, and J. Balakrishnan, Biophys. J. **91**, 1925 (2006).
7. J. Dostálek, J. Homola, and M. Miler, Sens. Actuators, B **107**, 154 (2005).
8. J. Cao, Y. Sun, Y. Kong, and W. Qian, Sensors **19**, 405 (2019).
9. K. V. Sreekanth, Y. Alapan, M. ElKabbash, E. Ilker, M. Hinczewski, U. A. Gurkan, A. De Luca, and G. Strangi, Nat. Mater. **15**, 621 (2016).
10. J. González-Colsa, G. Serrera, J. M. Saiz, F. González, F. Moreno, and P. Albella, Opt. Express **29**, 13733 (2021).
11. S. Nazem, M. Malekmohammad, and M. Soltanolkotabi, Appl. Phys. B: Lasers Opt. **126**, 96 (2020).
12. Y. Jourlin, S. Tonchev, A. V. Tishchenko, and O. Parriaux, IEEE Photonics J. **6**, 1 (2014).
13. J. Sauvage-Vincent, Y. Jourlin, V. Petiton, A. V. Tishchenko, I. Verrier, and O. Parriaux, Opt. Express **22**, 13314 (2014).
14. E. Laffont, N. Crespo-Monteiro, A. Valour, P. Berini, and Y. Jourlin, Sensors **23**, 1188 (2023).
15. K. Ichihashi, Y. Mizutani, and T. Iwata, Opt. Rev. **21**, 728 (2014).
16. J. Chandezon, D. Maystre, and G. Raoult, J. Opt. **11**, 235 (1980).
17. N. Lyndin and B. Usievich, "Modal and C Methods Grating Design and Analysis Software," 2013, https://mcgrating.com/.
18. E. Popov, L. Tsonev, and D. Maystre, J. Mod. Opt. **37**, 367 (1990).
19. A. V. Tishchenko and O. Parriaux, IEEE Photonics J. **7**, 1 (2015).
20. H. Bruhier, I. Verrier, T. Gueye, C. Varenne, A. Ndiaye, O. Parriaux, C. Veillas, S. Reynaud, J. Brunet, and Y. Jourlin, Opt. Lett. **47**, 349 (2022).
21. K. P. Birch and M. J. Downs, Metrologia **30**, 155 (1993).